EXOPLANETS

Cloudy mornings and clear evenings on a gas giant exoplanet

Sagnick Mukherjee[1,2,3]*, David K. Sing[1,4], Guangwei Fu[1], Kevin B. Stevenson[5], Stephen P. Schmidt[1], Harry Baskett[6], Mei Ting Mak[6,7], Patrick McCreery[1], Natalie H. Allen[1], Katherine A. Bennett[4], Duncan A. Christie[8], Carlos Gascón[9,10], Jayesh Goyal[11,12], Éric Hébrard[6], Joshua D. Lothringer[13], Mercedes López-Morales[13], Jacob Lustig-Yaeger[5], Erin M. May[5], L. C. Mayorga[5], Nathan Mayne[6], Lakeisha M. Ramos Rosado[1], Henrique Reggiani[14], Zafar Rustamkulov[4], Kevin C. Schlaufman[1], Kristin S. Sotzen[5], Daniel Thorngren[1], Le-Chris Wang[1], Maria Zamyatina[6]

The spectra of exoplanet atmospheres are affected by aerosols (clouds and hazes) of uncertain origin. Proposed aerosol formation mechanisms include gas condensation or photochemical reactions. We measured the transmission spectrum of the tidally locked gas giant exoplanet WASP-94A b and identified asymmetry in its atmosphere. The morning limb is cooler and cloudy, whereas the evening limb is hotter and exhibits gaseous water absorption features. We interpret this difference as being due to the formation of cloud droplets near the morning limb, which evaporate during circulation to the evening limb. The dominant aerosols are clouds cycling between the day and night sides of the atmosphere, not photochemical hazes. The resulting asymmetry can severely bias chemical abundance measurements, unless limb-resolved spectroscopy is available.

Aerosols are ubiquitous in the atmospheres of planets in the Solar System (*1*) and have been observed in exoplanet atmospheres (*2*–*4*). Aerosols affect the observed spectra of exoplanet atmospheres by muting gaseous absorption features, introducing additional spectral features, and changing the continuum slope (*3*, *5*–*7*). Physically, aerosols can cause atmospheric heating or cooling and alter atmospheric chemistry. There is limited information about the nature of these aerosols, their three-dimensional (3D) atmospheric distribution, or the physical processes that determine their properties. It is debated whether aerosols in the atmospheres of highly irradiated gas giant exoplanets (known as hot Jupiters) are predominantly clouds formed through condensation of minerals from atmospheric gases (*7*, *8*) or hazes produced by photochemical reactions driven by ultraviolet (UV) radiation from the host star (*9*–*11*).

The physical processes that govern aerosols in hot Jupiters—3D atmospheric circulation, aerosol response to temperature, and UV irradiation—are uncertain inputs to atmospheric models of these planets (*12*–*15*). Simulations predict that atmospheric circulation can transport aerosols across large fractions of the planet's circumference or the depth of its atmosphere (*12*, *13*, *14*) and that aerosols respond to 3D temperature gradients through evaporation, condensation, and chemical reactions (*16*–*18*). Theoretical estimates of the circulation timescales and aerosol particle sizes are uncertain by orders of magnitude (*19*, *20*).

Several observational techniques have been used to investigate aerosols, including phase-curve observations, which probe the emission from an exoplanet at different orbital phases (*5*, *21*). Infrared phase-curves constrain the 3D structure of exoplanet atmospheres, but if the atmosphere contains abundant aerosols, then this technique leads to degeneracies between the inferred thermal and cloud properties (*22*, *23*). Observations at high spectral resolution (known as limb-resolved spectroscopy) have spatially separated the limbs (the leading and trailing terminators) of exoplanet atmospheres. Those studies have shown chemical asymmetry between the limbs of some hot Jupiters (*4*, *24*), which might be due to condensation of gases in the colder night side of the planet. However, that technique does not directly probe aerosols, so alternative physical mechanisms have been proposed to explain these asymmetries (*25*, *26*).

Limb-resolved transmission spectroscopy at low spectral resolution (*27*–*29*) uses transit light curves (the stellar flux as a function of time as the exoplanet passes between the star and the observer) to separately measure the transit depths for the leading morning limb and the trailing evening limb of the planet (*30*, *31*). This technique has shown limb asymmetry in two gas giant exoplanets, driven by temperature difference between the limbs (*27*, *28*). Those studies did not find signatures of scattering driven by aerosols in either limb.

Uncertainties in aerosol physics limit our understanding of the formation and evolution of a wide variety of exoplanetary systems. The chemical compositions of exoplanets are typically inferred from measurements of their atmospheres (*32*, *33*), but key uncertainties in the aerosol physics can bias these measurements (*34*–*36*).

Observations of WASP-94A b

The hot Jupiter exoplanet WASP-94A b (also cataloged as CD-34 14724 Ab) has a mass of 0.456 Jupiter masses ($M_{\rm Jupiter}$) and a radius of 1.72 Jupiter radii ($R_{\rm Jupiter}$) (*37*). We observed a single transit of WASP-94A b with the Near Infrared Imager and Slitless Spectrograph (NIRISS) instrument on the James Webb Space Telescope (JWST) to obtain low-resolution time-resolved spectra covering 0.8 to 2.8 μm (*38*). We constructed white light curves of the transit in two broadband wavelength ranges—0.9 to 1.2 and 1.35 to 1.5 μm, which both cover strong H_2O absorption features—using the Fast InfraRed Exoplanet Fitting Lyghtcurve Suite (FIREFLy) analysis pipeline (*38*, *39*). We then fitted the data using two models with different assumed planet shapes: a spherically symmetric model and a model with limb-to-limb asymmetry (*30*, *31*, *38*). We initially fitted only the 0.9- to 1.2-μm band to constrain the planetary system parameters, including the mid-transit time (T_0) in each model. We then used the best-fitting T_0 values from the 0.9- to 1.2-μm light curve as fixed parameters in the model fitting of the 1.35- to 1.5-μm band in both models.

Figure 1A shows the observed light curve and both best-fitting models for the 1.35- to 1.5-μm band. The residuals for the asymmetric limb model (Fig. 1B) were consistent with zero, whereas those of the spherical planet model (Fig. 1C) showed substantial deviations during ingress and egress. We calculated that the data prefer the asymmetric limb model over the spherical limb model with a statistical significance of 6σ (*38*), indicating asymmetric transit depths for the two limbs.

The NIRISS spectroscopic light curves were binned to a spectral resolving power $R \sim 50$, and then we fitted the light curve at each wavelength using the asymmetric limb transit model (*38*). The light curve models at each wavelength were then used to derive a transmission

[1]William H. Miller III Department of Physics and Astronomy, Johns Hopkins University, Baltimore, MD, USA. [2]Department of Astronomy and Astrophysics, University of California, Santa Cruz, CA, USA. [3]School of Earth and Space Exploration, Arizona State University, Tempe, AZ, USA. [4]Department of Earth & Planetary Sciences, Johns Hopkins University, Baltimore, MD, USA. [5]Johns Hopkins Applied Physics Laboratory, Laurel, MD, USA. [6]Department of Physics and Astronomy, University of Exeter, Exeter, UK. [7]Sub-Department of Atmospheric, Oceanic, and Planetary Physics, University of Oxford, Oxford, UK. [8]Max Planck Institute for Astronomy, Heidelberg, Germany. [9]Center for Astrophysics, Harvard University and the Smithsonian, Cambridge, MA, USA. [10]Institut d'Estudis Espacials de Catalunya, Barcelona, Spain. [11]School of Earth & Planetary Sciences, National Institute of Science Education and Research, Jatni, India. [12]Homi Bhabha National Institute, Training School Complex, Anushaktinagar, Mumbai, India. [13]Space Telescope Science Institute, Baltimore, MD, USA. [14]Gemini Observatory, National Optical-Infrared Astronomy Research Laboratory, National Science Foundation, La Serena, Chile. ***Corresponding author. Email: smukhe50@asu.edu**

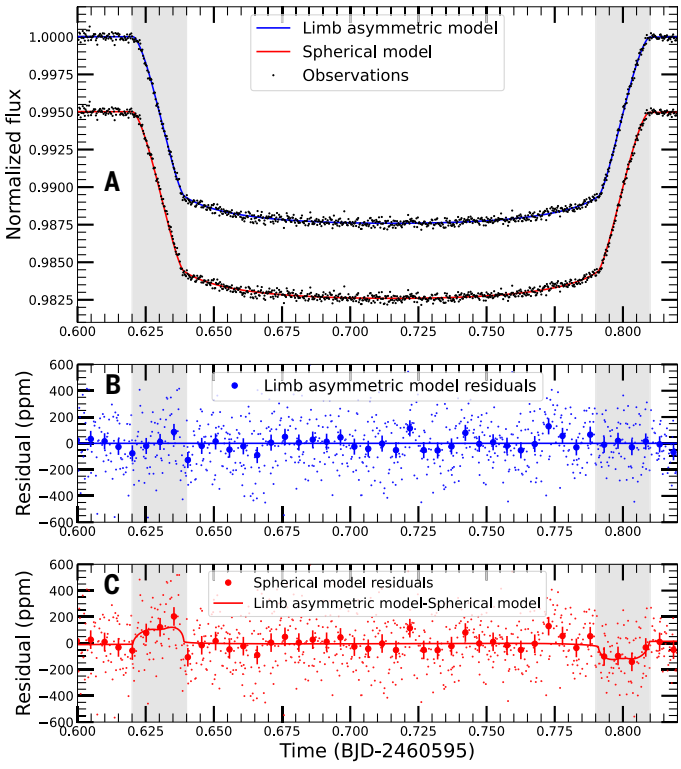

Fig. 1. Transit light curves of WASP-94A b and fitted models. (**A**) Black points are the observed broadband 1.35- to 1.5-μm light curve, plotted twice with a constant vertical offset. These light curves are overlain with the fitted models assuming a spherical planet (red line) or allowing for asymmetric limbs (blue line). Time is in Barycentric Julian Date (BJD), and the gray shaded regions are the ingress and egress. (**B**) Small blue data points represent the residuals between the asymmetric limb model and the data. Large blue data points are the residuals binned in time, with error bars showing their 1σ uncertainty. The residuals are consistent with zero (blue line). (**C**) Same as (B), but for the spherical planet model. This model is inconsistent with zero during the ingress and egress. The red line shows the difference between the asymmetric limb and spherical models. ppm, parts per million.

spectrum for each limb separately. Because hot Jupiters, such as WASP-94A b, are expected to be tidally locked to their host stars (*40*), we identified the leading morning limb and the trailing evening limb during the ingress and egress (Fig. 2A). The resulting transmission spectra of the two limbs are shown in Fig. 2, C and D. To check the results from FIREFLy, we also used two independent data analysis pipelines (Eureka! and Fu) to extract the morning and evening limb transmission spectra (*38*). The spectra from all three pipelines were consistent with each other (fig. S8).

The transmission depth offset between the morning and evening limb spectra depends on the precision of the T_0 measurement (*41*). We used archival observations of another transit of WASP-94A b using JWST's Near Infrared Spectrograph (NIRSpec) (*42*) to improve the precision of our T_0 measurement (*38*). We measured the extent by which the offset between the morning and evening limb spectra might change owing to our measured T_0 and accounted for this uncertainty within our modeling analysis (*38*). Star spots or faculae can also contaminate the transmission spectra of exoplanets (*43*). We investigated this effect using archival observations of the host star WASP-94A by the Transiting Exoplanet Survey Satellite (TESS), finding negligible contamination of our observed transmission spectra by spots or faculae (*38*).

Asymmetry caused by clouds, not hazes

The morning limb spectrum has no prominent gas absorption features and a sloped continuum, rising at shorter wavelengths, which is a signature of high-altitude aerosols (*44*). The evening limb spectrum does exhibit absorption features, consistent with gaseous H_2O (*38*), but has no substantial evidence of aerosols. This difference implies that the dominant aerosols on WASP-94A b are clouds, not hazes.

Hazes are theoretically expected to be preferentially produced on the UV-irradiated permanent day side (because WASP-94A b is tidally locked) and then transported to other parts of the atmosphere by planet-wide atmospheric circulation (*11*, *12*). Large haze particles (particle radius $r > 30$ nm) would therefore be more abundant on the evening limb than the morning limb (*19*), opposite to what we observed. Small haze particles ($r < 30$ nm) can be concentrated more on the morning limb (*19*, *45*). However, theoretical modeling of several hot Jupiters shows that this overconcentration in the morning limb is insufficient to completely suppress gas absorption features in the morning limb while maintaining prominent absorption features on the evening limb at the wavelengths of our observations (*45*).

Clouds are predicted to form in the cooler night side of the planet and then circulate downwind to the morning limb (*14*, *16*). Further transport to the much hotter day side is predicted to cause a large fraction of the cloud droplets to evaporate (*14*). This would cause the evening limb to be clearer than the morning limb, as we observed. We used a 3D general circulation model (GCM) to theoretically predict the atmospheric structure of WASP-94A b (*38*) without fitting the observed spectra. The GCM predicted cloud formation on the night side, with a clear evening and a cloudy morning limb (Fig. 2B). By fitting the morning limb spectrum with atmosphere models that include various types of aerosols, we found that clouds provide a better fit to the morning limb spectrum than do several potential haze species (*38*).

Temperature variations and diurnal cycles

We constructed an atmospheric model consisting of two separate atmospheric columns with distinct temperature and cloud structures, representing the morning and evening limbs (*38*). The temperature profiles of the two columns are required to converge in the deep atmosphere, based on theoretical predictions (*13*, *14*). We used this atmospheric model to fit the transmission spectrum of both limbs using a Bayesian atmospheric retrieval framework (*38*). The best-fitting retrieved theoretical model is compared to the observed spectra in Fig. 2, C and D. We found that the evening spectrum was dominated by H_2O absorption, which was detected with a significance of 10σ (*38*). The morning limb spectrum was dominated by cloud absorption, which was detected with 9σ significance (*38*).

Figure 3A shows the retrieved temperature-pressure [T(P)] profiles of each limb compared with theoretically calculated condensation curves (*8*) of three potential cloud species at the temperatures of WASP-94A b: Fe, $MgSiO_3$, and MnS. The T(P) profile of the evening limb is hotter than that of the morning limb, with a temperature difference of 449 ± 83 K, which crosses the condensation curves at low pressure (corresponding to high altitude). We therefore expected that any cloud droplets present at high altitudes on the morning limb would be evaporated at the same altitudes on the evening limb. We calculated the pressure ranges that contribute to the morning and evening limb spectrum (*38*) using contribution functions derived for transmission spectroscopy (*46*). Figure 3B shows that the morning limb spectrum probes pressures $\lesssim$0.01 mbar, whereas the evening limb spectrum probes 0.01 to 4 mbar. Figure 3B also shows the predicted T(P) profiles from the 3D GCM, which match the measured temperature difference between the limbs (*38*).

Figure 3 also shows the retrieved cloud properties of each limb. Figure 3, C and D, shows the cloud optical depth profiles, which indicate that the evening limb becomes transparent at pressures $\lesssim$1 mbar, but the morning limb remains optically thick until ~0.01 mbar (corresponding

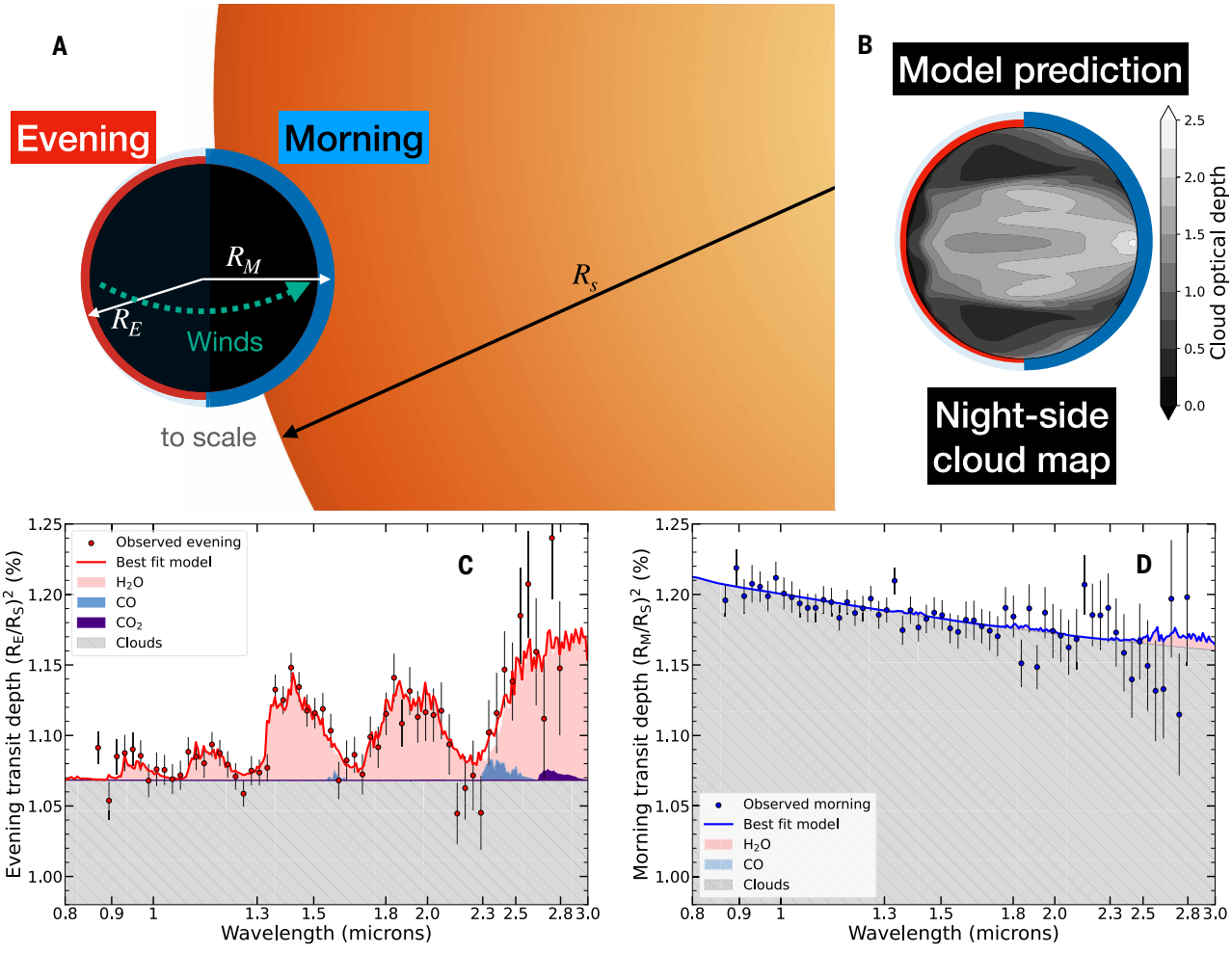

Fig. 2. Observing geometry, model predictions, and transmission spectra of the morning and evening limbs. (**A**) Diagram of the geometry of WASP-94A b and its host star (to scale) during the NIRISS observations. The red and blue regions represent the evening and morning limbs of the planet, respectively. The radii of the evening limb (R_E), morning limb (R_M), and the star (R_S) are indicated with white and black arrows. The dotted cyan arrow shows the direction of the equatorial jet predicted by theoretical models. (**B**) The night side cloud map of WASP-94A b predicted by the GCM. Grayscale shading represents the predicted optical depth of clouds; colored regions are the same as in (A). (**C**) Data points show the observed transmission spectrum of the evening limb, with 1σ error bars, on a nonlinear wavelength scale. The red line shows the best-fitting model from our atmospheric retrieval analysis. The shaded regions represent the model contributions from H_2O (pink), CO (light blue), CO_2 (dark indigo), and clouds (gray hatched). (**D**) Same as (C) but for the morning limb.

to a higher altitude). The retrieved temperature difference between the planet's limbs is sufficient to drive cloud cycling between the day and night sides (*38*), producing the difference in the cloud optical depth between the limbs and hence the observed H_2O absorption features. Figure 3, E and F, shows the mean cloud droplet sizes for the three cloud species at each limb; we found that the morning limb has droplets with a mean radius of 0.1 to 1 μm in the 0.01 to 1 mbar pressure range.

The distribution of cloud droplets is thought to be connected to atmospheric circulation timescales, including the vertical mixing and horizontal advection timescales (*47*, *48*). To constrain the strength of vertical mixing, we considered the balance between vertical lifting of cloud droplets and their gravitational settling, assuming steady state (*38*). Vertical mixing is quantified by the 1D vertical eddy diffusion parameter K_{zz}; we derived $\log_{10}\left(K_{zz}/\mathrm{cm^2 s^{-1}}\right) = 11.73 \pm 0.87$. This was consistent with the average altitude-dependent K_{zz} profile predicted by the GCM (*38*). The resulting vertical mixing timescale was ~0.06 to 4 days. If the horizontal advection timescale at 0.01 mbar was much slower than the vertical mixing timescale, then cloud droplets were stable at these high altitudes. However, if the horizontal advection timescale was faster, then cloud droplets were not replenished quickly enough to be maintained at high altitude in the morning limb.

The GCM predicts an equatorial jet that extends across the day and night sides of WASP-94A b (*38*). The fastest advection timescale (which governs horizontal transport of the cloud droplets from the morning to the evening limb) is within this equatorial jet, typically ~1.15 to 2.2 days. The jet in the GCM spans latitudes ±40° for pressures <1 bar. If the cloud droplets trace the wind velocities of the jet at higher altitudes in the GCM, then the vertical mixing timescale must be closer to 0.06 days than to 4 days.

Compositional measurement effects

To approximate the spectrum that would have been observed if we had not resolved the two limbs, we derived a planet-wide spectrum using the spherically symmetric model (*38*), which is shown in Fig. 4A. This unbinned spherical spectrum has absorption features owing to H_2O and an additional absorption feature that is not reproduced by our atmospheric model. We identified the latter as outflowing

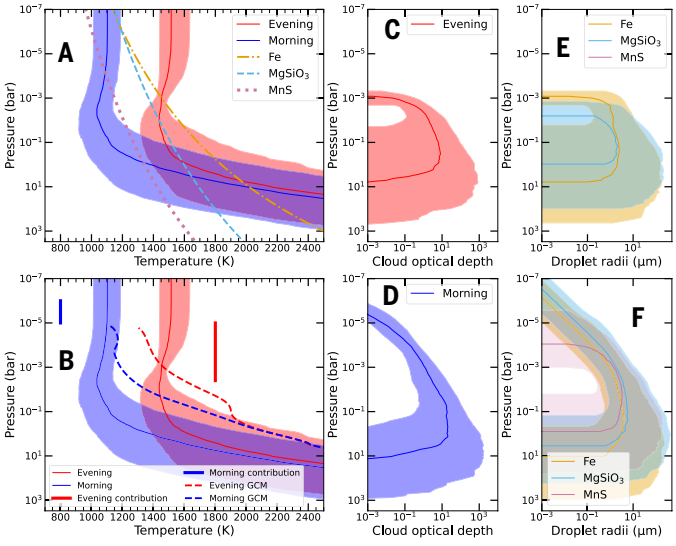

Fig. 3. Retrieved temperature and cloud structure of the morning and evening limbs. (**A**) Retrieved *T*(*P*) profiles for the morning (blue) and evening (red) limbs; lines represent the median values, and shading represents the 1σ uncertainty. Lines represent theoretical condensation curves for $MgSiO_3$ (dashed cyan), Fe (dot-dashed orange), and MnS (dotted purple) clouds. (**B**) The same retrieved *T*(*P*) profiles as in (A) but compared with the predictions from the GCM (dashed lines). The vertical red and blue bars show the range of pressures probed by the evening and morning limb spectra, respectively, calculated from the contribution function of the best-fitting retrieved model (*38*). (**C** and **D**) The retrieved cloud optical depth profiles at 1.5-μm wavelength for the evening and morning limbs. (**E** and **F**) The retrieved mean droplet radius profiles for the evening and morning limbs. Lines represent the median profiles, with shaded regions showing 1σ uncertainty, for $MgSiO_3$ (cyan), Fe (orange), and MnS (purple) clouds.

metastable helium, which has an absorption line at 1.083 μm (*38*). The presence of this species indicates rapid atmospheric mass loss from WASP-94A b (*38*).

We binned the spherical spectrum to the same resolving power as the asymmetric limb spectra for further analysis. The absorption features in the binned spherical spectrum are muted by a factor of ~2, compared with that of the evening limb spectrum. We then applied a retrieval method that models the spectrum with only one atmospheric column compared with the two atmospheric columns used for the limb-resolved spectra; the two modeling frameworks are otherwise identical. Figure 4, C to E, shows the resulting constraints on the chemical composition and cloud properties from the limb-resolved and spherical spectra.

The constraints on metallicity [M/H] [the logarithmic abundance of elements heavier than helium (M) relative to the abundance of hydrogen (H)] for WASP-94A b are [M/H] = +0.46 ± 0.36 from the limb-resolved observations and [M/H] = +1.937 ± 0.073 from the spherical spectrum. These values are inconsistent at statistical significance >4σ. We found that not accounting for the limb asymmetry biases the inferred metallicity. This bias was theoretically predicted (*34*); it arises from the dilution of gas absorption features in the spherical spectrum. The inferred carbon-to-oxygen (C/O) ratios (Fig. 4D) remain consistent but have different probability distributions for the same reasons. Figure 4E shows that K_{zz} is also affected by this bias, with the inferred values differing by 3σ. We also applied another retrieval method to the spherical spectrum, which linearly combines spectra from fully cloudy and fully clear atmospheric columns using a cloud-coverage fraction parameter (*38*). We found that this approach doesn't alleviate these biases (*38*).

We caution that this bias is unlikely to be limited to this planet or to similar hot Jupiters. Figure 4B shows the amplitude of the 1.4-μm H_2O absorption features measured by previous observational studies

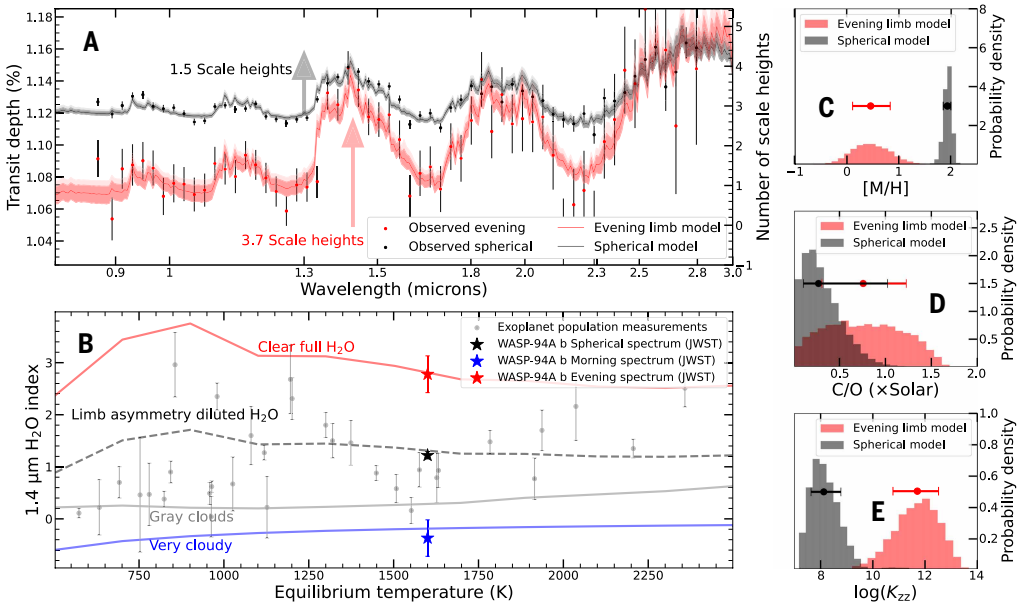

Fig. 4. Inferred composition of WASP-94A b and the effect of limb asymmetry. (**A**) The observed transmission spectrum of the evening limb (red points) compared with the average spectrum extracted assuming that the planet is spherically symmetric (black points). Lines are the median retrieved model spectra, with shaded regions showing their 1σ uncertainties. The right axis shows the number of atmospheric pressure scale heights probed by the observations, calculated using the equilibrium temperature, gravity, and retrieved atmospheric mean molecular weight. The length of the vertical arrows shows the amplitude of the 1.4-μm H_2O absorption feature relative to the continuum for the evening (pink) and spherical (gray) spectra. (**B**) Amplitude of the 1.4-μm H_2O absorption feature compared with previous observations of other exoplanets (*49*) (light gray points). Star symbols indicate the measured amplitude for WASP-94A b using the spherical spectrum (black) or the separate morning (blue) and evening (red) spectra. Lines are the H_2O amplitudes predicted by self-consistent atmospheric models assuming a clear atmosphere (red), a very cloudy atmosphere (blue), an atmosphere with clouds that have wavelength-independent absorption (gray), and an atmosphere with limb asymmetry (gray dashed). (**C**) The inferred atmospheric metallicity probability distributions (histograms) determined from the limb-resolved (red) and spherical (gray) spectra. Data points show the median values, which differ by 4σ. (**D** and **E**) Same as (C) but for the C/O ratio and K_{zz}, respectively. All error bars in this figure represent 1σ uncertainties.

of transiting exoplanets with a variety of sizes, masses, and temperatures (*49*). These H_2O amplitudes were all measured from the 1D spherical spectra without accounting for limb asymmetry. The H_2O amplitude we measure from the spherical spectrum of WASP-94A b follows the same trend as other hot Jupiters (temperatures of 1000 to 2000 K). However, our separate measurements for the two limbs of WASP-94A b are at the extremes of the range observed in other hot Jupiters. We calculated the spherical planet H_2O feature amplitude from a grid of fully clear and very cloudy 1D atmospheric models and a grid of models with one clear and one very cloudy limb (as we inferred for WASP-94A b) (*38*). If other hot Jupiters also have asymmetric limbs due to day-night cloud cycling, then these models imply that their H_2O feature would be diluted to varying levels, potentially biasing the inferred composition and cloud properties. We expect similar issues to apply to smaller exoplanets, such as sub-Neptunes, which are theoretically predicted to have substantial aerosol cover (*5*, *21*).

REFERENCES AND NOTES

1. K. H. Baines *et al.*, *Planet. Space Sci.* **57**, 1650–1658 (2009).
2. D. K. Sing *et al.*, *Nature* **529**, 59–62 (2016).
3. J. Inglis *et al.*, *Astrophys. J. Lett.* **973**, L41 (2024).
4. D. Ehrenreich *et al.*, *Nature* **580**, 597–601 (2020).
5. E. M. R. Kempton *et al.*, *Nature* **620**, 67–71 (2023).
6. P. Gao *et al.*, *Astrophys. J.* **951**, 96 (2023).
7. H. R. Wakeford, D. K. Sing, *Astron. Astrophys.* **573**, A122 (2015).
8. C. Visscher, K. Lodders, B. Fegley Jr., *Astrophys. J.* **716**, 1060–1075 (2010).
9. C. C. Porco *et al.*, *Nature* **434**, 159–168 (2005).
10. A. Sánchez-Lavega *et al.*, *Nat. Commun.* **11**, 2281 (2020).
11. E. M. R. Kempton, J. L. Bean, V. Parmentier, *Astrophys. J. Lett.* **845**, L20 (2017).
12. M. E. Steinrueck *et al.*, *Astrophys. J.* **951**, 117 (2023).
13. V. Parmentier, A. P. Showman, Y. Lian, *Astron. Astrophys.* **558**, A91 (2013).
14. S. Lines *et al.*, *Mon. Not. R. Astron. Soc.* **488**, 1332–1355 (2019).
15. D. A. Christie *et al.*, *Mon. Not. R. Astron. Soc.* **506**, 4500–4515 (2021).
16. V. Parmentier, J. J. Fortney, A. P. Showman, C. Morley, M. S. Marley, *Astrophys. J.* **828**, 22 (2016).
17. A. Arfaux, P. Lavvas, *Mon. Not. R. Astron. Soc.* **515**, 4753–4779 (2022).
18. A. Arfaux, P. Lavvas, *Mon. Not. R. Astron. Soc.* **530**, 482–500 (2024).
19. M. E. Steinrueck *et al.*, *Mon. Not. R. Astron. Soc.* **504**, 2783–2799 (2021).
20. T. D. Komacek, A. P. Showman, V. Parmentier, *Astrophys. J.* **881**, 152 (2019).
21. L.-P. Coulombe *et al.*, *Nat. Astron.* **9**, 512–525 (2025).
22. B. Burningham *et al.*, *Mon. Not. R. Astron. Soc.* **470**, 1177–1197 (2017).
23. P. Mollière *et al.*, *Astron. Astrophys.* **640**, A131 (2020).
24. T. Louden, P. J. Wheatley, *Astrophys. J. Lett.* **814**, L24 (2015).
25. A. B. Savel *et al.*, *Astrophys. J.* **944**, 99 (2023).
26. A. B. Savel *et al.*, *Astrophys. J.* **926**, 85 (2022).
27. N. Espinoza *et al.*, *Nature* **632**, 1017–1020 (2024).
28. M. M. Murphy *et al.*, *Nat. Astron.* **8**, 1562–1574 (2024).
29. J. J. Fortney *et al.*, *Astrophys. J.* **709**, 1396–1406 (2010).
30. K. Jones, N. Espinoza, *J. Open Source Softw.* **7**, 2382 (2022).
31. N. Espinoza, K. Jones, *Astron. J.* **162**, 165 (2021).
32. K. I. Öberg, R. Murray-Clay, E. A. Bergin, *Astrophys. J. Lett.* **743**, L16 (2011).
33. L. Welbanks *et al.*, *Astrophys. J. Lett.* **887**, L20 (2019).
34. M. R. Line, V. Parmentier, *Astrophys. J.* **820**, 78 (2016).
35. N. Madhusudhan, *Annu. Rev. Astron. Astrophys.* **57**, 617–663 (2019).
36. C. Mai, M. R. Line, *Astrophys. J.* **883**, 144 (2019).
37. M. Neveu-VanMalle *et al.*, *Astron. Astrophys.* **572**, A49 (2014).
38. Materials and methods are available as supplementary materials.
39. Z. Rustamkulov, D. K. Sing, R. Liu, A. Wang, *Astrophys. J. Lett.* **928**, L7 (2022).
40. A. P. Showman, T. Guillot, *Astron. Astrophys.* **385**, 166–180 (2002).
41. M. M. Murphy, T. G. Beatty, D. Apai, *Astrophys. J.* **974**, 179 (2024).
42. E.-M. Ahrer *et al.*, *Mon. Not. R. Astron. Soc.* **540**, 2535–2554 (2025).
43. D. K. Sing *et al.*, *Mon. Not. R. Astron. Soc.* **416**, 1443–1455 (2011).
44. A. Lecavelier Des Etangs, F. Pont, A. Vidal-Madjar, D. Sing, *Astron. Astrophys.* **481**, L83–L86 (2008).
45. M. T. Mak *et al.*, *Mon. Not. R. Astron. Soc.* **542**, 1873–1900 (2025).
46. Z. Rustamkulov *et al.*, *Nature* **614**, 659–663 (2023).
47. A. S. Ackerman, M. S. Marley, *Astrophys. J.* **556**, 872–884 (2001).
48. P. Gao, B. Benneke, *Astrophys. J.* **863**, 165 (2018).
49. G. Fu *et al.*, *Astrophys. J. Lett.* **847**, L22 (2017).
50. S. Mukherjee, Data from paper "Cloudy mornings and clear evenings on a gas giant exoplanet", Mikulski Archive for Space Telescopes (2025); https://doi.org/10.17909/eptp-qq05.
51. S. Mukherjee *et al.*, Cloudy mornings and clear evenings on a gas giant exoplanet. Zenodo (2025), https://doi.org/10.5281/zenodo.15085825.
52. E.-M. Ahrer, Data from "Tracing the formation and migration history: molecular signatures in the atmosphere of misaligned hot Jupiter WASP-94Ab using JWST NIRSpec/G395H", Mikulski Archive for Space Telescopes (2025); https://doi.org/10.17909/gsq8-zc73.
53. S. Mukherjee, Data for paper "Cloudy mornings and clear evenings on a gas giant exoplanet", Mikulski Archive for Space Telescopes (2026); https://doi.org/10.17909/m83w-8w86.
54. S. Mukherjee, FIREFLy v1.0.0, Zenodo (2026); https://doi.org/10.5281/zenodo.18616758.
55. The Eureka! Team, Eureka! v1.2, Zenodo (2025); https://doi.org/10.5281/zenodo.19076001.
56. G. Fu, Tswift v1, Zenodo (2026); https://doi.org/10.5281/zenodo.18636325.

ACKNOWLEDGMENTS

S.M. thanks J. Fortney, K. Ohno, and N. Roy for discussion and feedback. We thank the anonymous reviewers, whose feedback helped improve this manuscript. S.M. acknowledges use of the Lux supercomputer at University of California, Santa Cruz, which was funded by National Science Foundation (NSF) Major Research Instrumentation grant AST 1828315. H.B., N.M., É.H., and M.Z. acknowledge use of the Monsoon2 system, a collaborative facility supplied under the Joint Weather and Climate Research Programme, a strategic partnership between the Met Office and the Natural Environment Research Council. This work is based on observations made with the National Aeronautics and Space Administration (NASA)/European Space Agency/Canadian Space Agency JWST. The data were obtained from the Mikulski Archive for Space Telescopes at the Space Telescope Science Institute, which is operated by the Association of Universities for Research in Astronomy, Inc., under NNASA contract NAS 5-03127 for JWST. **Funding:** S.M. was supported by the Templeton Theory-Experiment (TEX) Cross Training Fellowship from the John Templeton Foundation and the 51 Pegasi b postdoctoral fellowship from the Heising-Simons Foundation. S.P.S. was supported by the NSF Graduate Research Fellowship Program under grant no. DGE2139757. H.B., M.T.M., N.M., É.H., and M.Z. acknowledge support from a Science and Technology Facilities Council Astronomy observation and theory small award (grant no. ST/Y00261X/1). N.M. was also supported by a United Kingdom Research and Innovation Future Leaders Fellowship (grant no. MR/T040866/1). M.T.M. acknowledges funding from the Bell Burnell Graduate Scholarship Fund (grant no. BB005) administered and managed by the Institute of Physics. P.M. and K.C.S. were supported by NASA under grant no. 80NSSC23K0266 issued through the Exoplanets Research Program (XRP). D.K.S. received support from JWST GO program number 5924 through a grant from the Space Telescope Science Institute, which is operated by the Association of Universities for Research in Astronomy, Inc., under NNASA contract no. NAS 5-03127. **Author contributions:** S.M. performed the FIREFLy data reduction of the observations. S.M. led the asymmetric limb atmospheric retrievals, performed the aerosol species retrievals, and led manuscript preparation. D.K.S. was the principal investigator of the JWST program and oversaw the development of the FIREFLy data reduction pipeline and its associated data analysis. D.K.S. also contributed to atmospheric modeling, theoretical interpretations, and manuscript preparation. G.F. and K.B.S. performed independent data reductions. S.P.S. performed the patchy cloud atmospheric retrievals on the spherical planet spectrum. H.B. and M.T.M. performed the GCM simulation, with contributions from N.M., M.Z., É.H. and D.A.C. P.M. modeled the helium ouflow signature with contributions from K.C.S. and J.D.L. N.H.A. contributed to the stellar contamination analysis. M.L.-M., J.L.-Y., L.C.M., and J.G. contributed to the theoretical design and implementation of the two-column Bayesian atmospheric retrieval. K.B.S., G.F., N.H.A., K.A.B., C.G., L.M.R.R., L.-C.W., E.M.M., D.T., Z.R., and H.R. modified and updated the data reduction and analysis pipelines for this work. K.B.S., G.F., S.P.S., H.B., P.M., N.H.A., K.A.B., D.A.C., C.G., J.G., E.H., M.L.M., E.M.M., L.C.M., N.M., L.M.R.R., H.R., Z.R., D.T., L.-C.W., M.Z., and M.T.M. contributed to manuscript preparation. M.T.M., K.B.S., N.H.A., J.D.L., J.L.-Y., E.M.M., L.C.M., L.M.R.R., K.C.S., K.S.S., and D.T. contributed to revising the manuscript. N.H.A., K.A.B., C.G., L.M.R.R., L.-C.W., E.M.M., Z.R., and K.S.S. contributed to observation planning. G.F., K.B.S., N.H.A., K.A.B., J.G., J.D.L., M.L.-M., N.M., L.M.R.R., H.R., Z.R., and K.C.S. contributed to preparation of the JWST proposal. **Competing interests:** The authors declare that they have no competing interests. **Data, code, and materials availability:** The JWST NIRISS observations of WASP-94A b are available on the Mikulski Archive for Space Telescopes (MAST) through program no. 5924 (*50*). Our reduced transmission spectra of the morning and evening limbs, best-fitting models, atmospheric retrievals, and GCM outputs are archived at Zenodo (*51*). The JWST NIRSpec observations are available on MAST through program no. 3154 (*52*). The TESS observations are also available on MAST (*53*). The FIREFly data analysis pipeline is available at https://github.com/sagnickm/FIREFLy and archived at Zenodo (*54*). The Eureka! pipeline is available at https://github.com/kevin218/Eureka and archived at Zenodo (*55*). The Fu data analysis pipeline is available at https://github.com/guangweifu/Tswift/tree/main and archived at Zenodo (*56*). No physical materials were generated in this work.

SUPPLEMENTARY MATERIALS

science.org/doi/10.1126/science.adx5903
Materials and Methods; Figs. S1 to 24; Tables S1 to S7; References (*57*–*169*)

Submitted 26 March 2025; accepted 19 March 2026

10.1126/science.adx5903

Cloudy mornings and clear evenings on a gas giant exoplanet

Sagnick Mukherjee, David K. Sing, Guangwei Fu, Kevin B. Stevenson, Stephen P. Schmidt, Harry Baskett, Mei Ting Mak, Patrick McCreery, Natalie H. Allen, Katherine A. Bennett, Duncan A. Christie, Carlos Gascón, Jayesh Goyal, Éric Hébrard, Joshua D. Lothringer, Mercedes López-Morales, Jacob Lustig-Yaeger, Erin M. May, L. C. Mayorga, Nathan Mayne, Lakeisha M. Ramos Rosado, Henrique Reggiani, Zafar Rustamkulov, Kevin C. Schlaufman, Kristin S. Sotzen, Daniel Thorngren, Le-Chris Wang, and Maria Zamyatina

Science **392** (6800), . DOI: 10.1126/science.adx5903

Editor's summary

When an exoplanet transits (passes in front of its host star, as seen from Earth), some of the background starlight passes through its atmosphere, where it can be absorbed or scattered. Transit observations can therefore determine the exoplanet's atmospheric spectrum averaged over the morning and evening sides. Mukherjee *et al*. have observed a transit of a gas giant exoplanet orbiting a bright star with sufficient signal-to-noise to extract separate spectra for the morning and evening. They found that the morning atmosphere is cloudy, but the evening atmosphere is clear and has water absorption features. This asymmetry can bias atmospheric composition measurements that use averaged spectra. —Keith T. Smith